

Submillimeter observations of IC 10: the dust properties and neutral carbon content of a low metallicity starburst

Alberto D. Bolatto, James M. Jackson

Institute for Astrophysical Research, Department of Astronomy, Boston University, Boston
MA 02215

Christine D. Wilson

Department of Astronomy, McMaster University, Ontario, Canada

and

Gerald Moriarty-Schieven

Joint Astronomy Centre, Hilo, Hawaii

ABSTRACT

We present submillimeter observations of the Local Group, metal-poor, irregular dwarf galaxy IC 10, directly relevant to the interaction between interstellar medium and star formation activity in primeval galaxies. Using the JCMT, we have observed the fine structure neutral carbon transition ${}^3P_1 \rightarrow {}^3P_0$ at 492 GHz and the rotational $J = 3 \rightarrow 2$ transition of ${}^{12}\text{CO}$ and ${}^{13}\text{CO}$ in the most massive giant molecular cloud complex in this galaxy, IC 10-SE. We find that, although the $I_{[\text{CII}]} / I_{\text{CO}}$ ratio for this object is a factor of 4 larger than the typical Milky Way value, its [C I] to CO intensity ratio $I_{[\text{CI}]} / I_{\text{CO}} \simeq 18 \pm 2$ (in units of $\text{erg s}^{-1} \text{cm}^{-2} \text{sr}^{-1}$) is similar (only about 50% larger) to that of the Milky Way. Modelling of the behaviour of the [C II]/CO and [C I]/CO intensity ratios with metallicity indicates that, if C^+ and C^0 are chiefly produced by UV photodissociation in the PDR, both ratios should increase sharply with decreasing metallicity (and consequently diminished UV shielding; Bolatto, Jackson, & Ingalls 1999). These data then suggest a different origin for an important fraction of C^0 in these clouds, unrelated to photodissociation.

We have also mapped the 850 μm continuum in this region using SCUBA. Employing these data in conjunction with KAO and IRAM measurements we find that the 100 μm to 1300 μm continuum emission corresponds to a graybody with an extremely low emissivity exponent, $\beta \sim 0.5$. We conclude that this low exponent is most likely due to the destruction of small dust grains, brought about by the increased penetration of UV radiation in the low metallicity ISM. If a low emissivity exponent in the submillimeter is a general property

of metal-poor systems then the interpretation of millimeter and submillimeter surveys of high- z galaxies should be revised.

Subject headings: galaxies: individual (IC 10) — galaxies: ISM — galaxies: irregular — radio lines: ISM — dust

1. Introduction

IC 10, an irregular, low metallicity dwarf galaxy (IBm or “Magellanic Cloud” type), is one of the most active star-forming galaxies in the Local Group. Its galaxy-wide massive star surface density is comparable to that of the starburst regions of M 33 (Massey, Armandroff, & Conti 1992). Because IC 10 is a nearby system that in many ways resembles primeval galaxies (morphologically irregular, metal-poor, and very actively forming stars) we have targeted it for a study of the interstellar medium (ISM) at submillimeter wavelengths that has direct relevance to star formation at high redshifts. This galaxy, at a distance of 0.82 Mpc (Wilson et al. 1996), is comparable in mass and size to the Small Magellanic Cloud. Its metallicity ($12 + \log(\text{O}/\text{H}) = 8.17$, $Z/Z_{\odot} \simeq 1/6$ Lequeux et al. 1979) falls between that of the Large and the Small Magellanic Clouds.

IC 10 is an ideal laboratory to study the interaction between a metal-poor ISM and strong radiation fields. Metallicity greatly influences the composition and structure of the ISM, especially when intense UV fields are present. Photodissociation regions (PDRs) are those portions of the interstellar medium where UV radiation dominates the physical and chemical processes. Because low metallicity PDRs have fewer heavy elements their gas phase chemistry is altered, changing the equilibrium abundances of the molecular species (e.g., van Dishoeck & Black 1988; Lequeux et al. 1994). The deficiency of heavy elements also lowers the dust-to-gas ratio. This in turn allows the UV radiation to penetrate more deeply into the molecular material, thereby causing widespread photodissociation and photoionization. The interaction between the starburst and the ISM in a low metallicity system is thus maximized, as the UV photons permeate the ISM relatively unimpeded. Molecular hydrogen is largely unaffected by this enhanced UV radiation because of the strong H_2 self-shielding and the mutual shielding between coincident lines of H and H_2 (Abgrall et al. 1992), but CO is strongly photodissociated. Ionized carbon [C II] observations in IC 10 suggest the presence of vast quantities of molecular hydrogen not traced by CO clouds (Madden et al. 1997).

IC 10 is undergoing a burst of star formation, with the center of activity in its south-east portion. Nonthermal emission, probably arising from a collection of supernova

remnants (Yang & Skillman 1993), H₂O megamaser emission (Henkel, Wouterloot, & Bally 1986; Baan & Haschick 1994), one of the highest surface densities of Wolf-Rayet stars in the Local Group (Massey et al. 1992) and one of the largest FIR luminosities among dwarf galaxies (Melisse & Israel 1994) all suggest current vigorous star formation activity. The ratio of WC types (He burning Wolf-Rayet stars) to WN types (CNO cycle Wolf-Rayet stars) is also unusually high. This has been interpreted as an initial mass function skewed towards higher stellar masses (Massey & Armandroff 1995).

Neutral hydrogen maps of IC 10 show a complex structure characterized by many peaks and holes, an extended low brightness halo, and a complex velocity field (Shostak 1974; Shostak & Skillman 1989 ; Wilcots & Miller 1998). The brightest H I peak is located in the southern part of the galaxy and it is associated with a cluster of H II regions (Hodge & Lee 1990) and a molecular cloud complex named IC 10-SE (Becker 1990). The center of star formation activity in IC 10 is located in close proximity to this H I column density maximum.

The CO emission from IC 10 is relatively weak, as is usual in dwarf irregular galaxies (e.g., Tacconi & Young 1987), many of which appear to be deficient in molecular gas although quite actively forming stars. CO was first detected by Henkel et al. (1986). The molecular cloud complexes have been mapped using single dish observations by Ohta, Sasaki, & Saitō (1988) and Becker (1990), and interferometrically by Wilson & Reid (1991), Ohta et al. (1992) and Wilson (1995). The CO intensity to H₂ column density conversion factor X_{CO} strongly depends on the metallicity of the clouds (Wilson 1995; Arimoto, Sofue, & Tsujimoto 1996; Israel 1997). This dependency explains why some dwarf irregular galaxies appear to be forming stars much more efficiently than the Milky Way; much of their molecular gas is not well traced by CO.

In this paper we present observations of the [C I] ($J = 1 \rightarrow 0$) and CO ($J = 3 \rightarrow 2$), two of the most important submillimeter cooling lines of the ISM, together with the dust continuum of the molecular cloud complex IC 10-SE. Neutral carbon is the byproduct of the photodissociation of CO, created when UV photons impinge on the surfaces of molecular clouds. Thus the [C I] $^3\text{P}_1 \rightarrow ^3\text{P}_0$ fine structure transition is thought to trace the photodissociation region (PDR), the transition zone at low extinction ($A_v \sim 1\text{--}3$) where UV radiation dissociates the skin of CO clumps. The CO ($J = 3 \rightarrow 2$) rotational transition typically traces moderately warm ($T \sim 30$ K) and dense ($n \sim 4 \times 10^4$ cm⁻³) molecular gas, although determining a precise T and n requires detailed modelling of several spectral lines.

2. Observations and results

2.1. Spectroscopic observations

We observed the [C I] fine structure line at 492.1607 GHz, the ^{12}CO ($J = 3 \rightarrow 2$) rotational transition at 345.7960 GHz and the ^{13}CO ($J = 3 \rightarrow 2$) rotational line at 330.5879 GHz toward IC 10-SE using the 15 meter James Clerk Maxwell Telescope (JCMT) at Mauna Kea, Hawaii. These observations were performed in the remote observing mode, during 8 half shifts from 18 to 28 July 1997. Pointing and focus were checked at the beginning of each 4 hour long observing segment. Standard flux calibrators were observed before and after the IC 10 observations, and their intensities were found to be within 30% (3σ) of their accepted values. Calibration was performed every 20 minutes using the standard chopper wheel method with warm (ambient temperature) and cold loads.

The [C I] line was observed using the Rx2 SIS receiver, with $\eta_{mb} = 0.52$ and HPBW=10.8". The τ_{225} zenith opacity was in the range 0.04 to 0.05, resulting in system temperatures $T_{sys} = 2500 - 3500$ K. When the weather did not allow [C I] observations we switched to our backup program, observing CO ($J = 3 \rightarrow 2$) with the Rx3 SIS receiver, $\eta_{mb} = 0.64$ and HPBW=13.2". The τ_{225} opacity at this time was in the range 0.12 to 0.16 with corresponding system temperatures $T_{sys} = 800 - 1500$ K for ^{12}CO and $T_{sys} \simeq 1400$ K for ^{13}CO . The back-end was the Digital Autocorrelation Spectrometer (DAS). The [C I] observations were performed in the DAS 500 MHz bandwidth mode, resulting in a spectral resolution of 374 kHz (0.23 km s^{-1}). The CO observations were accomplished using the DAS 760 MHz bandwidth mode with a resolution of 750 kHz (0.65 km s^{-1}).

We observed [C I] towards 6 positions in the molecular cloud complex IC 10-SE. Three of them correspond to the three clumps identified by Wilson & Reid (1991) using CO ($J = 1 \rightarrow 0$) interferometric observations. The other three positions were arranged to obtain a slice across the complex, along an axis roughly oriented towards the nearest cluster of H II regions. The [C I] observations of clumps MC1, MC2 and MC3 on IC 10-SE (Wilson, & Reid 1991) were performed in position switching mode, switching 30' away in azimuth. The rest of the observations were performed in beam switching mode, chopping with the secondary mirror 180" away at a frequency of 1 Hz. This technique resulted in better baselines with no obvious problems of emission in the reference position.

First order baselines were removed from each spectrum and the individual 5 minute integrations were coadded. After averaging, the [C I] spectra were Hanning smoothed to 3 MHz ($\sim 1.85 \text{ km s}^{-1}$). The results are shown in Figure 1 and compiled in Tables 1 and 2.

2.2. Continuum observations

The Submillimetre Common User Bolometer Array (SCUBA) 850 μm and 1350 μm observations were performed in service mode during the nights of 27 September, 10 November and 23 December 1997. SCUBA’s 850 μm and 1350 μm beam sizes are respectively 14” and 18” (Holland et al. 1999). One 64-position jiggle map was obtained at 850 μm (Fig. 5), by imaging a field ~ 2.3 arcmin in diameter centered NE of the IC 10-SE molecular cloud complex and containing it, as well as several nearby H II regions (Hodge & Lee 1990). The observations were performed in three different sessions, with a typical zenith sky transmission at 850 μm of 70% ($\tau_{850} \simeq 0.4$). We used a chopper throw of 120” in azimuth, and the total accumulated integration time was 128 minutes. Pointing was checked before each observing session and found to be within 2”. Calibration was performed using Uranus and Mars.

Simultaneous 450 μm data were acquired using SCUBA’s short-wavelength array, but due to the poor weather ($\tau_{450} > 2$) these observations did not yield any useful data. The 1350 μm observations were performed using one of SCUBA’s photometric pixels, acquiring one point at a time in a five point map centered on IC 10-SE and chopping 60”, with an integration of 3 minutes per point. Only the center position ($\alpha_{1950} = 00^{\text{h}}17^{\text{m}}44^{\text{s}}.5$, $\delta_{1950} = 59^{\circ}00'22''$) yielded a significant detection with a flux density of 55 ± 5 mJy.

3. Discussion

3.1. Comparison with previous CO observations

In this section we compare our CO observations with existing single-dish and interferometric data of IC 10-SE. With this comparison we aim to: 1) refine our determinations of line ratios by improving the alignment of the maps and 2) discuss possible excitation gradients in the source.

Figure 2 shows a comparison of our observations with Wilson & Reid’s (1991) interferometric ^{12}CO ($J = 1 \rightarrow 0$) measurements convolved to the JCMT’s beam. The agreement is extremely good after displacing the OVRO map 2” to the north of its nominal coordinates. Such an offset can be caused by errors in the JCMT pointing model, which has a typical RMS of 1.5”, or poor phase calibration in the interferometric data which can introduce displacements of order half a synthesized beam. Although either telescope can be the source of this discrepancy, in this work we have chosen to move the OVRO map for convenience. To compute the $I_{[\text{CI}]} / I_{\text{CO}}$ ratios discussed in §3.2 we have used the displaced

OVRO data.

Although Petitpas & Wilson (1998) studied the CO excitation in this complex for the central position, our new data reveal the spatial distribution. Figure 3 shows the ratio of Planck-corrected peak antenna temperature (i.e., the temperature of a blackbody that would emit as much power as is detected by the antenna) for the $J = 3 \rightarrow 2$ and $J = 2 \rightarrow 1$ transitions (Becker 1990; IRAM 30 meter telescope), computed as,

$$T_A^{Planck} = \frac{T^*}{\ln\left(\frac{T^*}{T_A + J_\nu(T_{CMBR})} + 1\right)} \quad (1)$$

where $T^* = h\nu/k$ is the energy of the transition expressed in temperature units, T_A is the measured Rayleigh-Jeans antenna temperature, and $J_\nu(T_{CMBR}) = T^*/(\exp(T^*/T_{CMBR}) - 1)$ is the Cosmic Microwave Background contribution at the frequency of interest. Because both sets of observations have very similar beam sizes no convolution is necessary (note that the IRAM map is not Nyquist-sampled, therefore we are losing some spatial information). The Planck-corrected antenna temperature ratio is $T_{3\rightarrow 2}^{Planck}/T_{2\rightarrow 1}^{Planck} \approx 1$ ($T_{mb(3\rightarrow 2)}/T_{mb(2\rightarrow 1)} \sim 0.55\text{--}0.7$) throughout IC 10-SE, consistent with thermalized gas (i.e., gas with kinetic temperature equal to the excitation temperature, $T_{ex} = T_{kin}$) at a temperature higher than the excitation energy of the $J = 2$ level (i.e., $T_{kin} > 15$ K). Thermalization is most easily attained if the gas is optically thick.

The $^{12}\text{CO}/^{13}\text{CO}$ ratio of the integrated line intensities listed in Table 3 also suggests optically thick ^{12}CO gas at the positions of the three main molecular clumps (MC1, MC2 and MC3). Although there are no estimates of the $^{12}\text{C}/^{13}\text{C}$ abundance ratio in IC 10, the measured $^{12}\text{CO}/^{13}\text{CO}$ line ratio is ≈ 10 for each of the three clumps, much smaller than the typical $^{12}\text{C}/^{13}\text{C} \approx 50$ isotopic ratio in Galactic or LMC molecular clouds (e.g., Langer & Penzias 1990; Johansson et al. 1994). At the position SL2, however, no ^{13}CO is detected in spite of the strong ^{12}CO emission. This may be caused by a smaller CO optical depth at the edge of the complex, which is consistent with the lack of strong emission at the position of SL2 in the CO ($J = 1 \rightarrow 0$) interferometric map (Wilson & Reid 1991).

Table 2 shows that the linewidths of the ^{12}CO spectra are systematically larger than those of [C I] by a factor of ~ 2 at the positions of the main molecular clumps, while the [C I]/CO linewidth ratio decreases to ~ 1 for SL2, at the edge of the complex. The broadening of spectral lines in the ISM is usually attributed to either optical depth or Doppler (turbulent) effects such those in macroturbulent models (e.g., Wolfire, Hollenbach & Tielens 1993). The linewidth ratios are thus consistent with an increasing optical depth towards the center of the complex. In particular, the linewidth ratio of ~ 1 towards SL2 is

consistent with the lower CO optical depth deduced from the $^{12}\text{CO}/^{13}\text{CO}$ line ratio. If the line profiles are instead caused by macroturbulence the linewidths will be dominated by the clump-to-clump velocity dispersion. A [C I] linewidth systematically smaller than its CO counterpart can only be understood if the [C I] emission arises solely from a fraction of the clumps featuring a smaller velocity dispersion. This, in turn, would imply that the [C I] emitting clumps are localized within a distinct region inside our beam. The interpretation of the observed [C I] linewidths as arising from macroturbulence requires, however, optically thick [C I] emission from individual clumps which we consider extremely unlikely.

3.2. The [C I]/CO intensity ratio

As discussed in §1, the strong interaction between UV fields and the ISM in low metallicity environments leads us to expect that the photodissociation products of CO will be enhanced in these systems. Because low metallicity systems require a larger column of molecular gas to achieve the UV extinction at which CO begins to form ($A_V \sim 3$), we expect an increase in the [C I]/CO intensity ratio in metal-poor clouds compared with molecular clouds in the Milky Way (Bolatto et al. 1999).

There are few observations of [C I] in systems of low metallicity. Wilson (1997) measured the atomic carbon emission from four individual molecular clouds in M33, a galaxy with a well studied metallicity gradient. Wilson finds [C I]/CO integrated intensity ratios in the range 0.18–0.04 with an average $\simeq 0.1 \pm 0.03$ (intensities in $\text{erg s}^{-1} \text{cm}^{-2} \text{sr}^{-1}$). This ratio is very similar to that of Galactic clouds, and there is no apparent enhancement in the two clouds with lower metallicity. It is, however, difficult to interpret this result because of the lack of other diagnostics in these sources (e.g., [C II] measurements).

Using the convolved interferometric CO ($J = 1 \rightarrow 0$) data (Wilson & Reid 1991) we have computed the $I_{[\text{C I}]} / I_{\text{CO}}$ ratio for our 6 pointings (Table 2). The average integrated [C I]/CO intensity ratio for IC 10-SE is 0.23 ± 0.03 when the intensities are in Rayleigh-Jeans observational brightness units of K km s^{-1} , or equivalently 18 ± 2 when the intensities are expressed in units of $\text{erg s}^{-1} \text{cm}^{-2} \text{sr}^{-1}$. Notice that this ratio is in principle an upper limit, since part of the CO flux may be resolved out by the interferometer. This result is similar to the [C I]/CO ≈ 20 ratio observed by Stark et al. (1997) towards N159-W in the Large Magellanic Cloud, and $\sim 50\%$ larger than the COBE FIRAS Galaxy-wide ratio of ≈ 13 (Wright et al. 1991). Such similarity is surprising in light of the factor of 4 in metallicity spanned by these sources, and the disparity in their [C II] intensities. Bolatto et al. (1999) developed a model for the [C I]/CO intensity ratio as a function of metallicity. According to this model, a roughly constant [C I]/CO ratio is difficult to understand if most of the

neutral carbon is predominantly produced by UV and is thus located in the PDR, the size of which must obey relatively simple scaling laws with metallicity. In the context of this model we can only understand a constant [C I]/CO ratio if most of the C^0 is not produced by photodissociation but by other chemical processes (e.g., an enhanced charge exchange reaction $C^+ + S \rightarrow C + S^+$), either in the surfaces of CO clumps or well mixed within the CO cores. Otherwise we expect a sharp increase in the [C I]/CO ratio with decreasing metallicity, mostly owed to the decreasing size of the CO cores in the clumps. Such an increase is apparent in the data for the [C II]/CO ratio, not a surprise since the dominant C^+ source is clearly UV photodissociation. This dichotomy in the behaviour of C^+ and C^0 points to, in our opinion, different dominant origin mechanisms for C^+ and C^0 .

Figure 4 shows the variation in the [C I] to CO ($J = 3 \rightarrow 2$) ratio across the IC 10-SE complex. Both the ratio of integrated intensities and the ratio of peak intensities remain constant along the slice within the errors. This indicates that [C I] and CO emission are coextensive and we are not resolving the C^0 /CO transition, not a surprise given that the JCMT [C I] beam subtends ≈ 44 pc at the distance of IC 10. Towards the ends of the strip, at potentially interesting places to observe changes in the [C I]/CO ratio, the signals are very weak and we lack the signal-to-noise necessary to measure this ratio. In the case of IC 10-SE the peak intensity ratio is on average about twice the integrated intensity ratio, reflecting the difference in linewidths discussed in §3.1.

Using the observed intensities of [C II], [C I] and CO we can compute the relative abundances of the three dominant forms of carbon in this source. To this effect we will use Eqs. 20 from Bolatto et al. (1999), which are accurate to within factors of ~ 2 for [C I] and [C II] under a wide range of conditions. The observed [C I] and CO ($J = 1 \rightarrow 0$) integrated intensities for MC1 are $I_{[C\ I]} \cong 3.6 \times 10^{-7}$ and $I_{CO} \cong 2.2 \times 10^{-8}$ erg cm $^{-2}$ s $^{-1}$ sr $^{-1}$, measured in a 10.8" beam. The [C II] intensity observed by Madden et al. (1997) is $I_{[C\ II]} \cong 7.5 \times 10^{-5}$ erg cm $^{-2}$ s $^{-1}$ sr $^{-1}$, albeit in a 55" beam. The resulting column densities are $N_{CO} \cong 1.3 \times 10^{18}$, $N_{C^0} \cong 4.7 \times 10^{16}$, and $N_{C^+} \cong 5.9 \times 10^{16}$ cm $^{-2}$. Petitpas & Wilson (1998) obtained a somewhat larger column density $N_{CO} \cong 6 \times 10^{18}$ cm $^{-2}$ from a multiline excitation analysis, albeit in a larger beam (22") that only partially contains MC1 (it is displaced 14" from our position). Furthermore, using the total column density of hydrogen derived from the dust continuum measurements discussed in the following section (c.f., Table 5) the C relative abundance is $N_C/N_H \simeq 1.3 \times 10^{18}/2.8 \times 10^{22} = 4.6 \times 10^{-5}$. This is a factor of 4 smaller than the C abundance in a typical Milky Way cloud like ζ Oph (Duley & Williams 1984), which is consistent with the metallicity of IC 10-SE.

Therefore, unless there are strong local enhancements of N_{C^+} , CO is the dominant form of carbon in the molecular peaks of IC 10-SE. It has been found, however, that in

general CO is a poor tracer of molecular gas in dwarf galaxies as it is discussed in §1. For example, Mochizuki et al. (1994) find that the distribution of [C II] emission in the Large Magellanic Cloud is very different from the CO. Is this the case too in IC 10? IC 10-SE is the molecular peak of this galaxy and one of the few regions with enough extinction to form CO clouds (e.g., Becker 1990). The measurements by Madden et al. (1997) show other places in IC 10 with very large $I_{[\text{CII}]} / I_{\text{CO}}$ ratios (e.g., position D is a [C II] peak with no known CO counterpart). Thus, although locally CO is preponderant in IC 10-SE, C^+ is likely to be the globally dominant form of carbon in this galaxy.

3.3. The dust continuum

Dust grains heated by starlight are the main source of the FIR continuum emission. Since dust is also the source of UV extinction, it determines the distribution of the photodissociated gas. The thermal dust continuum contains information about the total mass of molecular gas and the radiation field that is heating the grains, which can be compared with estimates obtained by other methods. Finally, the emissivity law of the dust particles yields information on the composition of the dust grains and their size distribution. In this section we present the first determination of the submillimeter dust emissivity in a metal-poor system.

Figure 5 shows the thermal dust continuum at $850 \mu\text{m}$, imaged with SCUBA down to a 1σ sensitivity of $\sim 7.5 \text{ mJy/beam}$. The peak of the emission is coincident with the molecular cloud complex IC 10-SE, with a northern extension and a fainter SE-NW ridge of emission both associated with cluster of H II regions and in overall shape and dimensions very similar to the single dish CO $J=1 \rightarrow 0$ map (Becker 1990) and the 6 cm radio-continuum observations of Yang & Skillman (1993). Figure 6 shows the dust continuum overlaid on a deep optical (B band) picture of the galaxy. Not surprisingly, the peak of SCUBA emission is associated with an obscuration lane situated very close to the center of star formation activity in IC 10.

After convolving these observations to the resolution of previous FIR maps of this source ($\sim 50''$ HPBW, equivalent to $\sim 200 \text{ pc}$ at the adopted distance; Thronson et al. 1990), we find that the general morphology is well preserved although there is a displacement of order $30''$ between the 95 or $155 \mu\text{m}$ KAO data and the $850 \mu\text{m}$ SCUBA map (Fig. 7). Although the estimated 1σ positional uncertainty of the KAO data is $10''$, we consider that the observed displacement is an artifact of pointing. Notice that while the CO, C^+ and $850 \mu\text{m}$ peaks are all coincident, the best correlation between the FIR map in Thronson et al. and the C^+ and CO data is obtained only after such an offset is applied

to the FIR map (Madden et al. 1997). Unfortunately the IRAS HIRES maps of this region cannot be used to further clarify this point, since their positional accuracy is only about 30" (incidentally, the HIRES peak falls between the KAO and the SCUBA positions). The experience at KAO suggests that, while uncommon, such pointing errors are entirely possible. This is especially true during the observation of faint irregular galaxies when it is impossible to autoguide on the source itself (Harper 1999), as was the case for IC 10. Therefore, we consider that the 30" displacement is most likely a registration offset caused by an error in the KAO pointing, and in our continuum analysis we use the peak values of the source in each map. Using the nominal FIR values at the position of the 850 μm peak ($S_{95} = 17$ Jy, $S_{155} = 14$ Jy) only causes a moderate shift in the temperature of the solution, without altering the conclusions (the solution for the free-free corrected 95, 155, 850, and 1300 μm points would then be $T \simeq 38$ K, $\tau_{\text{mm}} \simeq 6.8 \times 10^{-5}$, $\beta \simeq 0.6$. The IRAS HIRES point at 60 μm cannot be used because of the uncertainty in its position).

To compare our submillimeter measurements with the FIR data it is necessary to convolve them to a common angular resolution. This is a problem for the 1350 μm data, for which we have only a single pointing with HPBW 18". To overcome this problem we include data from a 1.3 mm continuum map of IC 10 taken at IRAM. The corresponding flux density of this region is 280 mJy in a 50" beam (Wild 1998). The FIR/submillimeter measurements are summarized in Table 4.

For a modified blackbody (a graybody) the opacity τ_λ is a function of wavelength of the form

$$\tau_\lambda = \left(\frac{\lambda_0}{\lambda} \right)^\beta \quad (2)$$

where β is the graybody emissivity exponent, and λ_0 is the wavelength at which the emission becomes optically thick. Accordingly, the thermal emission from a graybody can be expressed as

$$S_\nu = \Omega B_\nu(T) \left(1 - e^{-\left(\frac{\lambda_0}{\lambda}\right)^\beta} \right) \quad (3)$$

where S_ν is the observed flux density, Ω is the source solid angle, and $B_\nu(T)$ is Planck's function. In the optically thin regime a simultaneous determination of the source size and opacity is impossible, and we can only determine the product $\Omega\tau_\lambda$. We set $\Omega = \Omega_{\text{beam}} = 6.7 \times 10^{-8}$ sr $^{-1}$ and the opacity thus determined is an average over the beam.

The dust opacity in the FIR-submillimeter regime is generally very small ($\tau \ll 1$). In

the optically thin limit the opacity is related to the hydrogen column density by $\tau_\lambda = b \sigma_\lambda N_{\text{H}}$ and thus

$$\frac{S_\nu}{\Omega} = b \sigma_\lambda N_{\text{H}} B_\nu(T) \quad (4)$$

where σ_λ is the dust opacity per hydrogen atom per cm^2 in the diffuse ISM (the canonical dust cross-section), b is a numerical factor (see below), and the hydrogen column density is $N_{\text{H}} = N(\text{H}) + 2N(\text{H}_2)$. The relationship between the opacity and the hydrogen column density can be expressed as

$$\tau_\lambda \simeq b \frac{Z}{Z_\odot} \sigma_{\text{mm}} \lambda_{\text{mm}}^{-\beta} N_{\text{H}} \quad (5)$$

where Z/Z_\odot is the metallicity of the gas relative to the Sun, σ_{mm} is the value of σ_λ at a wavelength of 1 mm and solar metallicity, λ_{mm} is the wavelength in mm and it is implicitly assumed that the dust-to-gas ratio is proportional to the metallicity. The numerical factor b is of order unity and depends on the grain environment: $b \approx 1$ for the dust in the diffuse interstellar medium considered by Draine & Lee (1984), $b > 1$ for dust in deeply embedded sources where ice mantles form on the grain surfaces, $b < 1$ in environments where grain destruction is occurring (Mezger, Wink, & Zylka 1990; Braine et al. 1997). Ossenkopf & Henning (1994) have modeled the opacity of interstellar grain aggregates in a variety of physical conditions applicable to protostellar cores (i.e., highly embedded sources). They find that for such sources the submillimeter opacity per unit dust mass can be a factor of 5 larger on average than in the diffuse interstellar medium, implying $b \sim 5$. The increased opacity in these environments is caused by the formation of thick ice mantles and the coagulation of fluffy particle aggregates (e.g., Fogel & Leung, 1998). The theoretical estimate for the dust opacity per hydrogen atom is $\sigma_{\text{mm}} = 7 \times 10^{-27} \text{ cm}^2$ in diffuse gas (Draine & Lee 1984), while observations place this number a factor of 1.2–1.7 higher in a wide range of objects (Braine et al. 1997, and references therein).

Figure 8 shows the measured flux density with the corresponding modified blackbody solutions. The solutions were computed using the 60, 95, 155, 850 and 1300 μm points listed in Table 4. The best-fit single temperature graybody solution to the flux density has a very shallow slope in the Rayleigh-Jeans limit, corresponding to a FIR-submillimeter emissivity exponent $\beta \sim 0.3$ at a temperature $T \simeq 60$ K with an opacity at 1 mm $\tau_{\text{mm}} \simeq 5 \times 10^{-5}$ (notice that this solution is slightly different from the median solution in the Monte Carlo listed in Table 5). Fitting the data with a blackbody produces $T \sim 85$ K and $\tau_{\text{mm}} \sim 4 \times 10^{-5}$. In fact, the slope derived from the 850 and 1300 μm measurements alone

is $\lambda^{-(2+\beta)} \simeq \lambda^{-2.16}$, very close to a blackbody. This extremely shallow emissivity is unusual. Grain emissivity exponents for different materials are thought to be in the range $1 < \beta < 2$, corresponding to amorphous ($\beta \simeq 1$) and metallic or crystalline ($\beta \simeq 2$) structure (e.g., Draine & Lee 1984; Tielens & Allamandola 1987; Mennella, Colangelli, & Bussoletti 1995). Astronomical measurements generally confirm this result for both Galactic (e.g., Knapp, Sandell, & Robson 1993) and extragalactic sources (e.g., Hughes, Gear, & Robson 1994).

The grain emissivity may be influenced by environmental characteristics, mainly the interstellar radiation field. IC 10-SE is in close proximity to the most luminous H II region in IC 10 (region 111, Hodge & Lee 1990). This region has an H_α flux of 2.8×10^{-13} erg s^{-1} cm^2 , and consequently a luminosity $L_{H_\alpha} \sim 4.5 \times 10^{37}$ erg s^{-1} (assuming an extinction correction $A_{H_\alpha} = 0.8$ and $D = 820$ kpc; Thronson et al. 1990; Wilson et al. 1996), or about four times as luminous as the Orion nebula (Kennicutt 1984). We can estimate the average radiation field in this region by assuming that all the starlight is reradiated in the FIR. Using our graybody solution, the observed FIR surface brightness is $S_{\text{FIR}} \approx 1.5 \times 10^{-9}$ erg s^{-1} cm^{-2} $beam^{-1}$, resulting in a flux $F_{\text{FIR}} \approx 0.30$ erg s^{-1} cm^{-2} . This is equivalent to an average radiation field $\chi_{uv} \simeq 190\chi_0$ over a region 200 pc in diameter, where χ_0 is the standard radiation field in the vicinity of the Sun ($\chi_0 = 1.6 \times 10^{-3}$ erg s^{-1} cm^{-2} ; Habing 1968). Most of the submillimeter emission comes from a region $\sim 22''$ (~ 90 pc) wide. Assuming that all the flux originates in that region, its radiation field is $\chi_{uv} \sim 900\chi_0$. This value is probably an underestimate, since we are neglecting: 1) the contribution of the stochastically heated small grains, which will produce excess radiation shortwards of $100 \mu\text{m}$ and increase the integrated FIR flux, and 2) the possibility that any form of radiation other than FIR is escaping the region (i.e., we assume 100% UV to FIR conversion efficiency). Nevertheless, this estimate is about a factor of four higher than the average radiation field in the Orion region where $\chi_{uv} \sim 250$ (over scales of tens of parsecs; Stacey et al. 1993) and agrees very well with estimates for χ_{uv} based on [C II] data for the same region (Madden et al. 1997).

Contamination by free-free radiation is a possible cause for a shallow long wavelength slope in the graybody solution. Optically thin thermal free-free emission has a flat spectrum ($S_\nu \propto \nu^{-0.1}$) that we can remove from the longer wavelength data to increase the slope of the graybody in the Rayleigh-Jeans limit. To obtain $\beta=1-2$ using solely the two longest frequency measurements, the contribution from the free-free radiation should be $S_\nu \simeq 120-190$ mJy at $\lambda \sim 1$ mm. One way to assess how much free-free is contaminating our fluxes is to simultaneously fit the graybody and the free-free emission (4 free parameters, 5 data points). Doing so results in only 7 mJy free-free at 1 mm, therefore we expect a rather small free-free contamination in our continuum data. Klein & Gräve (1986) found that the galaxy-wide flux density for IC 10 at 6.3 cm is 222 mJy with a spectral index

$\alpha \simeq -0.33$, slightly steeper than purely thermal bremsstrahlung radiation. The spectral index flattens to $\alpha = -0.1$ – -0.2 at the location of the two emission peaks, one of which appears to be associated to IC 10-SE (peak “B” for Klein & Gräve). Assuming $\alpha = -0.15$, these numbers predict a free-free contribution to the spectral density $S_\nu \simeq 120$ mJy at 1 mm, with roughly $2/3$ of the flux originating in the southernmost component identified with IC 10-SE. Therefore we assume $S_\nu^{ff} \approx 80 \lambda_{\text{mm}}^{0.15}$ mJy. Removing this contribution from the observed fluxes will raise β to about 0.5 when fitting all data points. Thus, we find that although contamination by bremsstrahlung radiation should be taken into account when deriving the graybody solution, it is not enough to bring the graybody emissivity exponent up to $\beta = 1$.

How much can we trust our determination of the submillimeter emissivity? We have performed a 10^4 points Monte Carlo analysis on the free-free corrected measurements, assuming independent gaussian errors with 3σ deviations according to Table 4 (the assumed 3σ deviations in flux correspond to 50% calibration errors). The results of this analysis are shown in Figure 9 and allow us to discard emissivity exponents $\beta \gtrsim 1$ as statistically very improbable. Another possible source of error is a bad data point, or a systematic calibration difference among the different telescopes. Eliminating the data from any one of the telescopes listed in Table 4, however, still results in an emissivity exponent very close to zero for the fit to the remaining data. Both KAO points, for example, need to be raised by a factor of ~ 2 to produce $\beta \sim 1$ when fitting all five measurements. Although this is not impossible, we find unlikely that a bad data point or a systematic calibration difference is causing our low β result.

A third possibility is the presence of a substantial mass of very cold dust in the line of sight. Since we have five measurements, we can fit a two temperature component graybody with an arbitrary emissivity. The results are summarized in Table 5. To determine if an important component of cold dust is a possibility we will compute the mass of cold dust and compare it to virial estimates for the mass of this region. Although a large mass of cold dust is consistent with the shape of the submillimeter continuum, such a cold dust component would contain so much mass that it is inconsistent with the observed column density of hydrogen. The H I distribution for IC 10 peaks in the IC 10-SE region, at a column density of $4.1 \times 10^{21} \text{ cm}^{-2}$ imaged with a 30” beam (Shostak & Skillman 1989). Single dish CO observations (Becker 1990), when corrected by metallicity effects (Wilson 1995), imply a molecular hydrogen column density $N(\text{H}_2) \simeq 9.3 \times 10^{21} \text{ cm}^{-2}$ for IC 10-SE (see also Petitpas & Wilson, 1998). The total column density of hydrogen is thus $N_{\text{H}} = N_{\text{HI}} + 2N_{\text{H}_2} \simeq 2.3 \times 10^{22} \text{ cm}^{-2}$. This figure agrees very well with the estimate based on the low emissivity graybody models setting $b \sim 1$ (c.f., Table 5), and is smaller than the column densities predicted by the two temperature models by about a factor

of 10. As we discussed before, highly embedded sources may have b as large as 5, which will diminish this discrepancy to a factor of about 2. The gas intermixed with such a cold dust component should be molecular and emit strongly in CO $J = 1 \rightarrow 0$ but little or nothing in the $J = 2 \rightarrow 1$ transition. Its emissivity will probably be about a factor of 4 smaller than the molecular gas associated with the warm component (i.e., the ratio of dust temperatures in the two components), and thus could be conceivably “masked” by the warmer gas associated with active star-forming regions. If we adopt the $\beta = 1.5$ two-temperature solution in Table 5 and proceed to correct down the expected N_{H} column density by a factor of $5 \times 4 = 20$, we obtain a cold CO ($J = 1 \rightarrow 0$) emissivity a factor of ~ 2 larger than that of the warm CO. Therefore, we should see about 3 times more flux in CO ($J = 1 \rightarrow 0$) than in CO ($J = 2 \rightarrow 1$).

We will compare now this expectation with observations. A multiline excitation analysis of IC 10-SE has been performed by Petitpas & Wilson (1998). No unique solution was found by the authors, which they attribute to the presence of two density components. Another possible explanation, however, would be the existence of two temperature components. The observed main beam line temperature ratio is $^{12}\text{CO} (J = 2 \rightarrow 1)/(J = 1 \rightarrow 0) = 0.64 \pm 0.05$, somewhat smaller than the typical line ratio for ^{12}CO in Milky Way clouds (about 0.8), but not as low as our reasoning in the previous paragraph leads us to expect. This is, however, further complicated by the fact that ^{12}CO is most probably optically thick. A more useful probe (but much more difficult to observe) would be an optically thin isotopomer like C^{18}O . There are also no signs of self absorption in the $^{12}\text{CO} (J = 1 \rightarrow 0)$ spectra (e.g., Becker 1990), as expected if some of the cold CO is located in front of the warm CO along the line of sight. Notice that this hypothetical very cold gas component cannot be the source of the excess [C II] emission observed by Madden et al. (1997) since the $158 \mu\text{m}$ transition requires 91 K to be excited. Hence, although we cannot conclusively discard the possibility a substantial mass of cold dust with the present data, we consider a two temperature model with a dominant cold dust fraction very unlikely and conclude that the submillimeter emissivity exponent of the dust in this environment is intrinsically small.

Thus, we have explored and find unlikely the possibility of calibration errors, free-free radiation and cold dust as the plausible causes of the low emissivity exponent that we observe in this source. Such a shallow emissivity must then be intrinsic, and related to some unique characteristic of IC 10-SE such as its low metallicity and high radiation field. Calculations show that for sufficiently small graphite grains the photon absorption cross-section Q_{abs}/a is independent of the grain size a and temperature T , as electric dipole absorption is the dominant mechanism (Draine & Lee 1984). For larger grains ($a \gtrsim 0.5 \mu\text{m}$) magnetic dipole absorption becomes important and Q_{abs}/a shows a strong temperature dependence for wavelengths longwards of $100 \mu\text{m}$, as well as a weaker dependence on λ which

translates into a shallower emissivity (c.f., Figure 4b of Draine & Lee 1984). Quantitatively, however, inspection of Figure 4b reveals that $\beta \sim 1.5$ for the largest and hottest graphite grains and $\beta \sim 1.8$ –2 otherwise (silicate grains and smaller graphite grains), values typical for crystalline materials. There are no similar calculations for amorphous carbonaceous materials, which laboratory measurements show to have $\beta \sim 0.8$ –1.3 (Menella et al. 1995). Hence, although theory suggests that a small β is possible if small grains are absent and the dust size distribution is dominated by large grains, there is no actual quantitative support for $\beta \sim 0.5$. Observational evidence for small grain destruction in starburst environments similar to IC 10-SE has been found by several studies, for example: PAH destruction in the core of M82 (Normand et al. 1995), gas phase silicon enhancement associated with silicate grain destruction by supernovae-driven shocks (Lord et al. 1996), FIR color-UV field correlation caused by small grain evaporation (Telesco, Decher, & Joy 1989; Boulanger et al. 1988), and metallicity effects on the FIR colors attributed to small grain destruction (Sauvage, Thuan, & Vigroux 1990). In view of this, we consider possible that the small emissivity exponent of the thermal dust continuum results from small grain destruction occurring in an actively star-forming low metallicity environment.

The continuum from the nucleus of M 82 has been studied in detail by Hughes et al. (1994), who found for it a normal emissivity exponent ($\beta = 1.3$) despite the high radiation field ($\chi_{uv} \sim 4700$ in the central region, $\chi_{uv} \sim 440$ over a larger extent; Stacey et al. 1991). It is important to keep in mind, however, that the metallicity of the nucleus of M 82 is about 14 times larger than the metallicity of IC 10 (Alloin et al. 1979). The ratio of χ_{uv}/Z is then ~ 3 times larger for IC 10-SE versus the central region of M 82. Naively, this would indicate a 3 times bigger “effective” radiation field (i.e., corrected by dust extinction) in IC 10. Without detailed modelling of the physical processes involved in grain formation and destruction, however, it is difficult to quantify the separate effects of Z and χ_{uv} on the grain size distribution. Nevertheless, it is important to point out that a high radiation field alone, such as the one found in the cores of starburst galaxies, may not be sufficient to produce as shallow an emissivity law as we observe in IC 10. Such a low β may require both low metallicity and a high radiation field.

This result, if confirmed, has potentially important implications for the recently opened field of continuum observations of young galaxies at high redshifts (e.g., Smail, Ivison, & Blain 1997; Barger et al. 1998; Barger, Cowie, & Sanders 1999) since it would affect the shape of their spectral energy distribution (SED) at long wavelengths. With equal T and τ_{mm} , a galaxy with smaller β will be brighter in the Rayleigh-Jeans portion of its continuum. Thus galaxy counting surveys would tend to be dominated by such sources, and backwards extrapolation from the current galaxy population using a standard SED with $\beta = 1.5$ may considerably underpredict the observed galaxy counts at high redshifts.

4. Summary

We have observed [C I], ^{12}CO and ^{13}CO ($J=3 \rightarrow 2$), and dust continuum in the SE region of IC 10. This is one of the few submillimeter neutral carbon studies of a metal-poor system (Stark et al. 1997; Wilson 1997).

We detected the [C I] 609 μm line towards four out of six positions in IC 10-SE, at the 3σ level or higher. All four points share a similar value of $I_{[\text{C I}]} / I_{\text{CO}} \simeq 18 \pm 2$ (in $\text{erg s}^{-1} \text{cm}^{-2} \text{sr}^{-1}$). This ratio is similar to that observed in the Orion region and most Milky Way sources ($I_{[\text{C I}]} / I_{\text{CO}} \sim 10\text{--}15$), and the N 159 region in the Large Magellanic Cloud ($I_{[\text{C I}]} / I_{\text{CO}} \simeq 20$), in spite of these regions spanning a factor of 4 in metallicity and a factor of 3 in $I_{[\text{C III}]} / I_{\text{CO}}$. The similarity of the $I_{[\text{C I}]} / I_{\text{CO}}$ ratio among sources of disparate metallicity is associated to the nature of the $\text{C}^+ / \text{C}^0 / \text{CO}$ transition in molecular clouds and possibly the structure of the clouds themselves (Bolatto et al. 1999; Pak et al. 1998). We believe that the observed trend of constant $I_{[\text{C I}]} / I_{\text{CO}}$ ratio with decreasing metallicity and increasing $I_{[\text{C III}]} / I_{\text{CO}}$ points to a non-PDR origin for most of the C^0 in molecular clouds. While the final settling of this question must necessarily await for better statistics, the hints offered by these observations are tantalizing.

The spectral energy distribution of the submillimeter continuum is relatively shallow, resulting in a graybody emissivity exponent $\beta \sim 0.5$. It is unlikely that this small emissivity exponent is caused by errors in the measurements, a miscalibration of one of the telescopes, contamination of the thermal greybody spectrum by free-free emission or a substantial amount of cold dust along the line of sight, therefore we believe it is intrinsic. Furthermore, the standard hydrogen column density estimate based upon the dust continuum emission agrees very well with the column density derived using other methods.

The physical cause of the shallow emissivity may be the destruction of small grains by UV radiation, which effectively penetrates farther into the ISM in low metallicity environments with low dust-to-gas ratios. This study of a nearby, low metallicity interstellar medium actively forming stars has direct relevance to present and future efforts to observe the young galaxy population at high redshifts.

The authors wish to thank D. P. Clemens for useful comments on the draft of this paper, as well as an anonymous referee for a very thorough job that definitely improved this work. The research of A.D.B. and J.M.J. was supported in part by the National Science Foundation through grant AST-9803065. The research of C.D.W. is supported through a grant from the Natural Sciences and Engineering Research Council of Canada. This research has made use of NASA’s Astrophysics Data System Bibliographic Services. The

JCMT is operated by the Royal Observatory Edinburgh on behalf of the Particle Physics and Astronomy Research Council of the United Kingdom, the Netherlands Organization for Scientific Research, and the National Research Council of Canada.

REFERENCES

- Abgrall, H., Le Boulrot, J., Pineau des Forêts, G., Roueff, E., Flower, D. R., & Heck, L. 1992, *A&A*, 253, 525
- Alloin, D., Collin-Souffrin, S., Joly, M., & Vigroux, L. 1979, *A&A*, 78, 200
- Arimoto, N., Sofue, Y., & Tsujimoto, T. 1996, *PASJ*, 48, 275
- Baan, W. A., & Haschick, A. 1994, *ApJ*, 424, L33
- Barger, A. J., Cowie, L. L., Sanders, D. B., Fulton, E., Taniguchi, Y., Sato, Y., Kawara, K., & Okuda, H. 1998, *Nature*, 394, 248
- Barger, A. J., Cowie, L. L., & Sanders, D. B. 1999, *ApJ*, 518, L5
- Becker, R. 1990, Ph. D. thesis, Universität Bonn
- Bolatto, A. D., Jackson, J. M., & Ingalls, J. G. 1999, *ApJ*, 513, 275
- Boulanger, F., Beichman, C., Désert, F. X., Helou, G., Pérault, M., & Ryter, C. 1988, *ApJ*, 332, 328
- Braine, J., Guélin, M., Dumke, M., Brouillet, N., Herpin, F., & Wielebinski, R. 1997, *A&A*, 326, 963
- Draine, B. T., & Lee, H. M. 1984, *ApJ*, 285, 89
- Duley, W. W. & Williams, D. A. 1984, *Interstellar Chemistry* (London:Academic Press), 9
- Fogel, M. E., & Leung, C. M. 1998, *ApJ*, 501, 175
- Habing, H. J. 1967, *Bull. Astron. Inst. Netherlands*, 19, 421
- Harper, D. A. 1999, priv. comm.
- Henkel, C., Wouterloot, J. G. A., & Bally, J. 1986, *A&A*, 155, 193
- Hodge, P., & Lee, M. G. 1990, *PASP*, 102, 26
- Holland, W. S., et al. 1999, *MNRAS*, 303, 659
- Hughes, D. H., Gear, W. K., & Robson, E. I. 1994, *MNRAS*, 270, 641
- Israel, F.P. 1997, *A&A*, 328, 471

- Johansson, L. E. B., Olofsson, H., Hjalmarsen, Å., Gredel, R., & Black, J. H. 1994, *A&A*, 292, 371
- Kennicutt, R. C. 1984, *ApJ*, 287, 116
- Klein, U., & Gräve, R. 1986, *A&A*, 161, 155
- Knapp, G. R., Sandell, G., & Robson, E. I. 1993, *ApJS*, 88, 173
- Langer, W. D., & Penzias, A. A. 1990, *ApJ*, 357, 447
- Lequeux, J., Peimbert, M., Rayo, J. F., Serrano, A., & Torres-Peimbert, S. 1979, *A&A*, 80, 155
- Lequeux, J., Le Bourlot, J., Pineau des Forêts, G., Roueff, E., Boulanger, F., & Rubio, M. 1994, *A&A*, 292, 371
- Lord, S. D., Hollenbach, D. J., Haas, M. R., Rubin, R. H., Colgan, S. W. J., & Erickson, E. F. 1996, *ApJ*, 465, 703
- Madden, S. C., Poglitsch, A., Geis, N., Stacey, G. J., & Townes, C. H. 1997, *ApJ*, 483, 200
- Magnani, L., & Onello, J. S. 1995, *ApJ*, 443, 169
- Massey, P., Armandroff, T. E., & Conti, P. S. 1992, *AJ*, 103, 1159
- Massey, P., & Armandroff, T. E. 1995, *AJ*, 109, 2470
- Melisse, J. P. M., & Israel, F. P. 1994, *A&ASS*, 103, 391
- Mennella, V., Colangeli, L., & Bussoletti, E. 1995, *A&A*, 295, 165
- Mezger, P. G., Wink, J. E., & Zylka, R. 1990, *A&A*, 228, 95
- Mochizuki, K. et al. 1996, *ApJ*, 430, L37
- Normand, P., Rouan, D., Lacombe, F., & Tiphene, D. 1995, *A&A*, 297, 311
- Ohta, K., Sasaki, M., & Saitō, M. 1988, *PASJ*, 40, 653
- Ohta, K., Sasaki, M., Yamada, T., Saitō, M., & Nakai, N. 1988, *PASJ*, 40, 653
- Ossenkopf, V., & Henning, Th. 1994, *A&A*, 291, 943
- Pak, S., Jaffe, D. T., van Dishoeck, E. F., Johansson, L. E. B., & Booth, R. S. 1998, *ApJ*, 498, 735
- Petitpas, G. R., & Wilson, C. D. 1998, *ApJ*, 496, 226
- N., Johansson, L. E. B., Stacey, G. J., & Sternberg, A. 1995, *ApJ*, 454, 293
- Sauvage, M., Thuan, T. X., & Vigroux, L. 1990, *A&A*, 237, 296
- Schralm, J., & Mezger, P. G. 1969, *ApJ*, 156, 269

- Shostak, G. S. 1974, *A&A*, 31, 97
- Shostak, G. S., & Skillman, E. D. 1989, *A&A*, 214, 33
- Smail, I., Ivison, R. J., & Blain, A. W. 1997, *ApJ*, 490, L5
- Stacey, G. J., Geis, N., Genzel, R., Lugten, J. B., Poglitsch, A., Sternberg, A., & Townes, C. H. 1991, *ApJ*, 373, 423
- Stacey, G. J., Jaffe, D. T., Geis, N., Genzel, R., Harris, A. I., Poglitsch, A., Stutzki, J., & Townes, C. H. 1993, *ApJ*, 404, 219
- Stark, A. A., Bolatto, A. D., Chamberlin, R. A., Lane, A. P., Bania, T. M., Jackson, J. M., & Lo, K.-Y. 1997, *ApJ*, 480, L59
- Tacconi, L. J., & Young, J. S. 1987, *ApJ*, 322, 681
- Telesco, C. M., Decher, R., & Joy, M. 1989, *ApJ*, 343, L13
- Thronson, H. A., Hunter, D. A., Casey, S., & Harper, D. A. 1990, *ApJ*, 355, 94
- Tielens, A. G. G. M., & Allamandola, L. J. 1987, in *Interstellar Processes*, eds. D. J. Hollenbach and H. A. Thronson (Reidel:Dordrecht), 397
- van Dishoeck, E. F., & Black, J. H. 1988, *ApJ*, 334, 771
- Wilcots, E. M., & Miller, B. W. 1998, *AJ*, 116, 2363
- Wild, W. 1998, priv. comm.
- Wilson, C. D. 1995, *ApJ*, 448, L97
- Wilson, C. D. 1997, *ApJ*, 487, L49
- Wilson, C. D., & Reid, I. N. 1991, *ApJ*, 366, L11
- Wilson, C. D., Welch, D. L., Reid, I. N., Saha, A., & Hoessel, J. 1996, *AJ*, 111, 1106
- Wolfire, M. G., Hollenbach, D. J., & Tielens, A. G. G. M. 1993, *ApJ*, 402, 195
- Wright, E. L. et al. 1991, *ApJ*, 381, 200
- Yang, H., & Skillman, E. D. 1993, *AJ*, 106, 1448

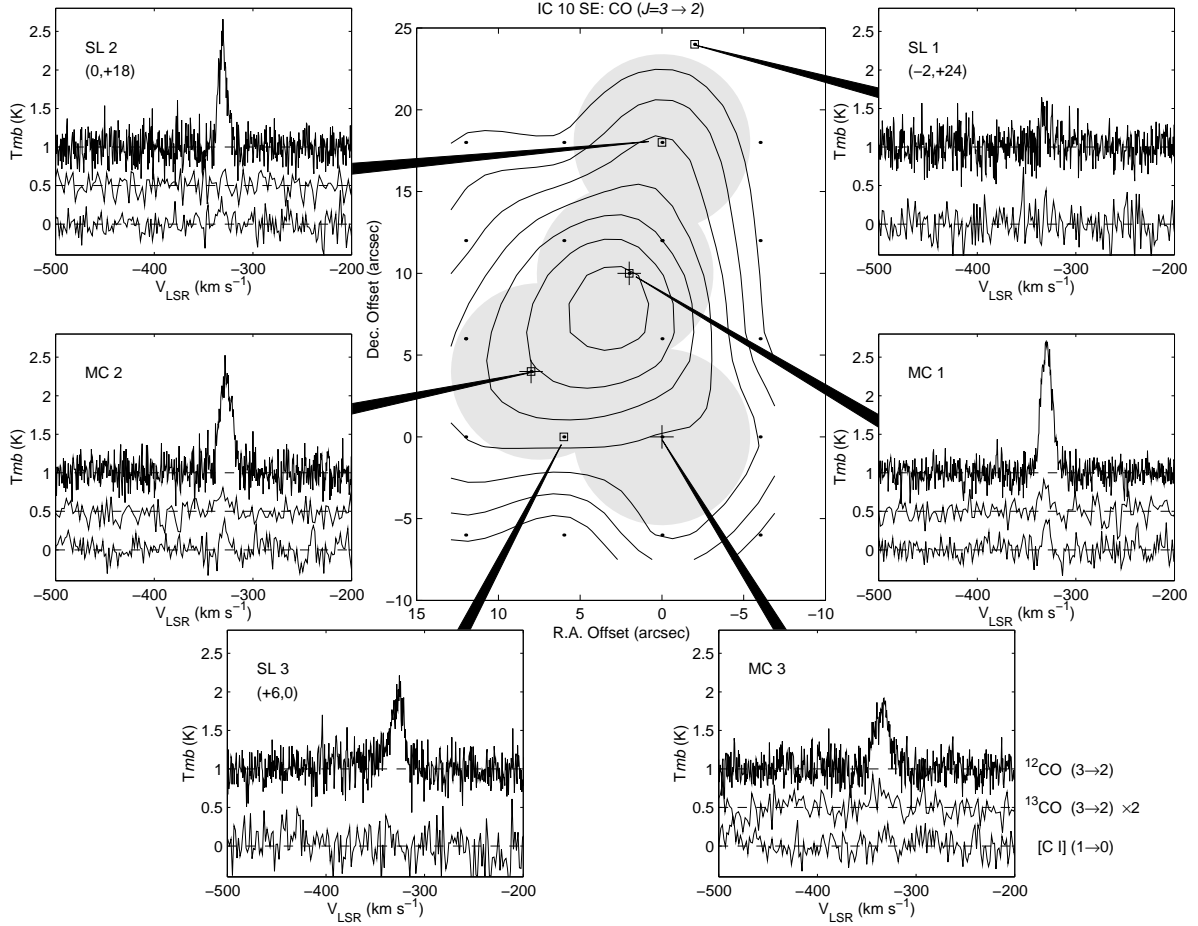


Fig. 1.— [C I] and CO ($J = 3 \rightarrow 2$) in IC 10-SE. The contour map shows the CO integrated intensity. The contour levels are 8 to 23 in steps of 2.5 K km s^{-1} , and the map offsets are with respect to MC3 (c.f., Table 1). The dots show the actual CO pointings that constitute the map. The crosses are placed at the positions of clumps identified by Wilson & Reid (1991). The squares show the placement of our slice observations, while the gray circles illustrate the size of the JCMT [C I] beam. Our six [C I] spectra (lower) are shown here together with the ^{12}CO (upper) and ^{13}CO ($J = 3 \rightarrow 2$) (middle) obtained towards the same positions. For display purposes, the ^{13}CO spectra are scaled by a factor of 2 and displaced 0.5 K, while the ^{12}CO spectral are displaced by 1.0 K.

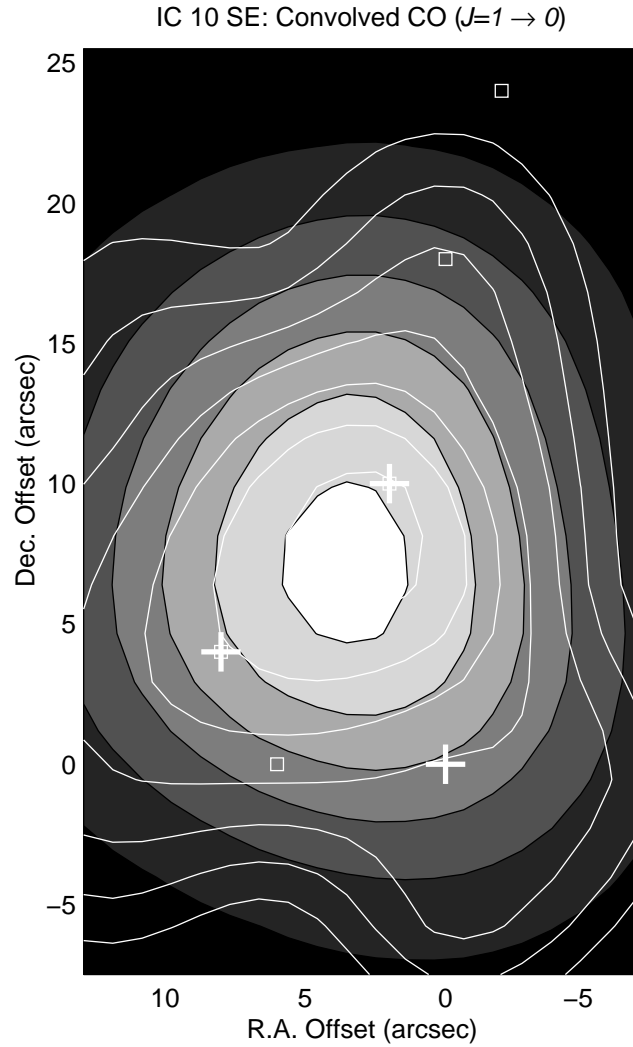


Fig. 2.— CO ($J = 3 \rightarrow 2$) contour map (white) overlaid on the OVRO interferometric CO ($J = 1 \rightarrow 0$) (Wilson & Reid 1991) convolved to the JCMT CO ($J = 3 \rightarrow 2$) beam (gray scale contours). The OVRO data has been displaced $2''$ to the north from its nominal coordinates. The OVRO contour levels are 2 to 12 in steps of 2 K km s^{-1} .

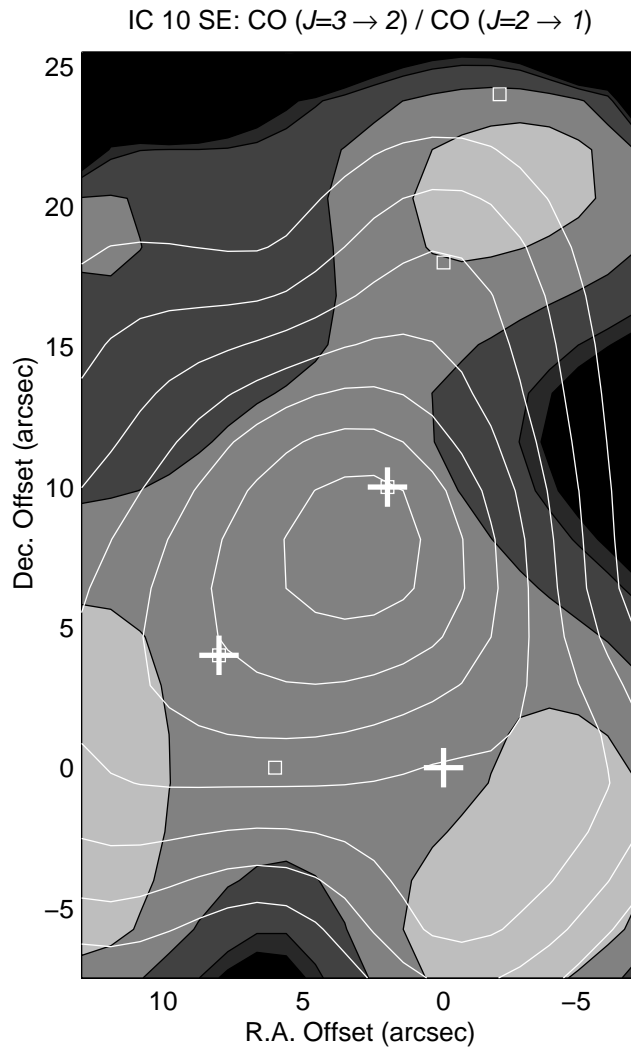


Fig. 3.— Planck-corrected peak antenna temperature ratio map for the CO ($J = 3 \rightarrow 2$) (this paper) and CO ($J = 2 \rightarrow 1$) (Becker 1990) transitions (grayscale) overlaid on the CO ($J = 3 \rightarrow 2$) integrated intensity map (white contours). Both data sets have very similar spatial resolution. The gray scale contours are 0.8 to 1.1 in steps of 0.1. This map shows that, within errors, the $J = 3 \rightarrow 2$ and $J = 2 \rightarrow 1$ transitions are probably optically thick and thermalized, and they trace the same gas throughout the complex.

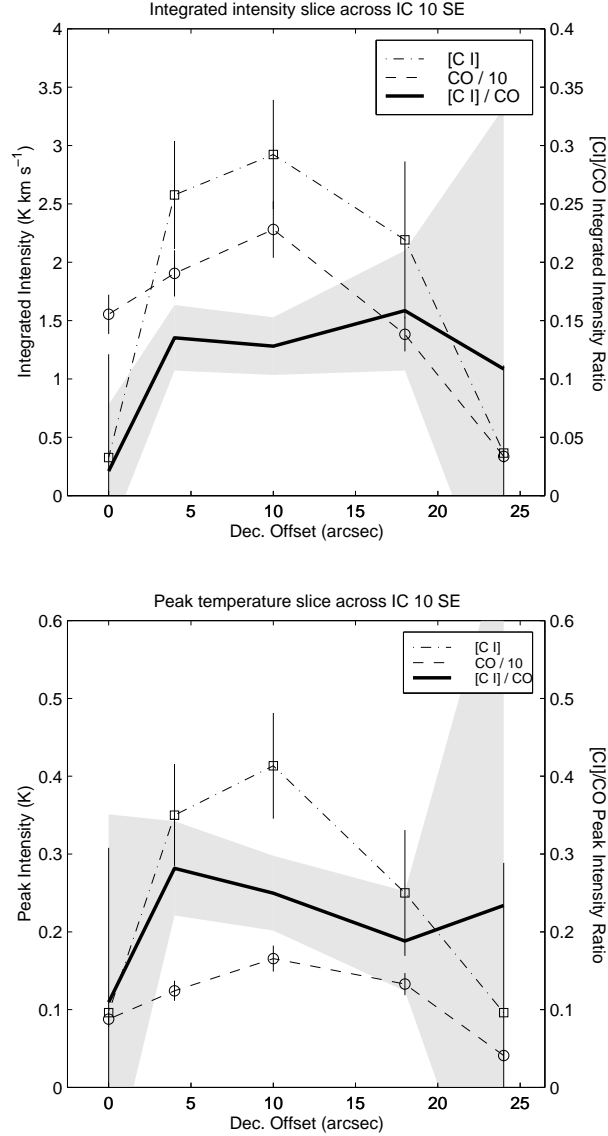


Fig. 4.— [C I] and CO ($J = 3 \rightarrow 2$) data in the slice across IC 10-SE. (*Top*) The squares correspond to the [C I] integrated intensity (scale is on the left vertical axis) and the circles correspond to the CO integrated intensity, scaled down by a factor of 10. The ratio $I_{[\text{C I}]} / I_{\text{CO}}$ along the slice is shown by the solid line (scale on the right vertical axis). The 1σ error bars have been computed including the internal errors as well as a 10% 1σ uncertainty in the calibration. (*Bottom*) Same as above but for the peak intensities along the slice. Both plots are compatible with an essentially constant ratio across IC 10-SE.

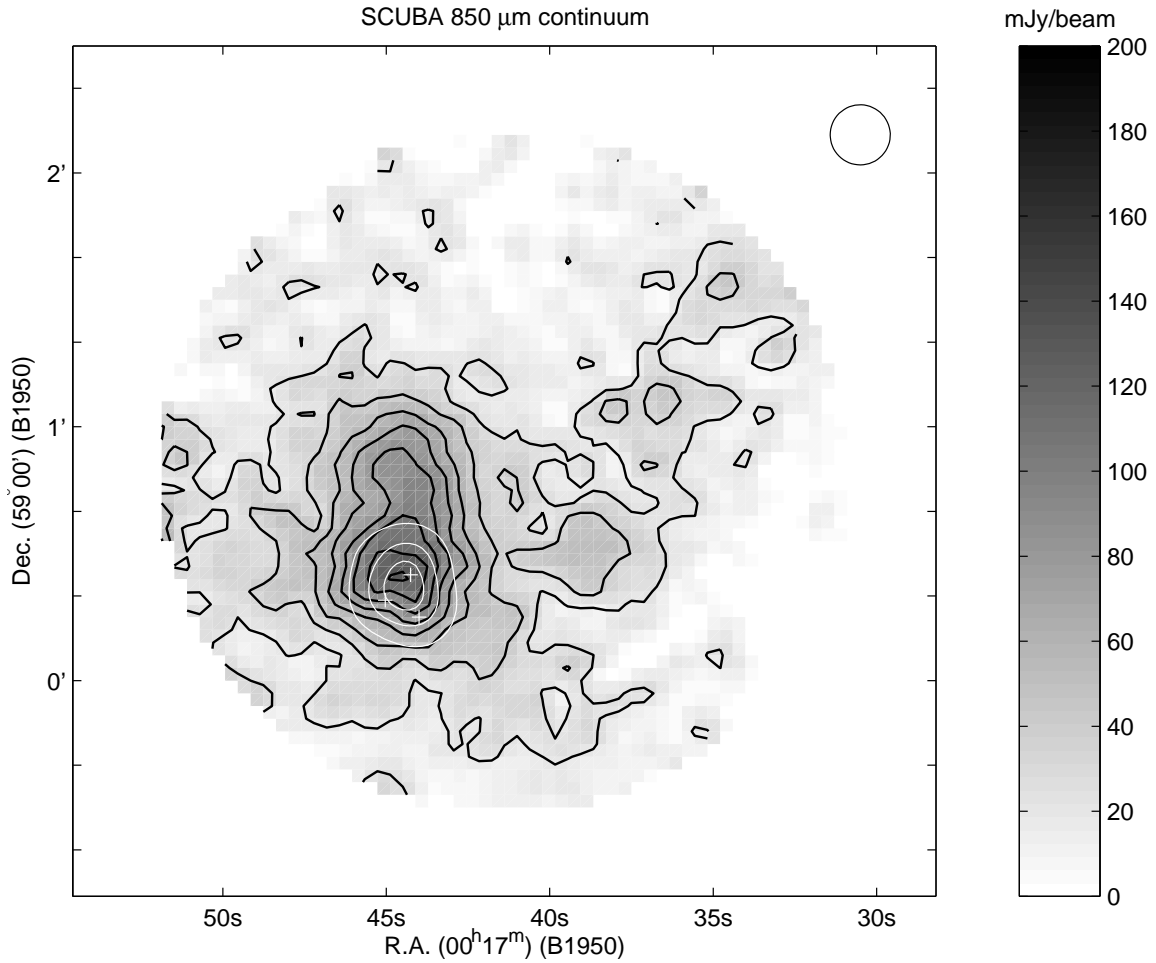


Fig. 5.— OVRO CO ($J = 1 \rightarrow 0$) contours (white) overlaid on our SCUBA 850 μm continuum map (grayscale). The circle in the upper right corner illustrates the size of SCUBA’s beam. The contour levels are 23 to 128 in steps of 15 mJy per beam ($1\sigma = 7.5$ mJy/beam).

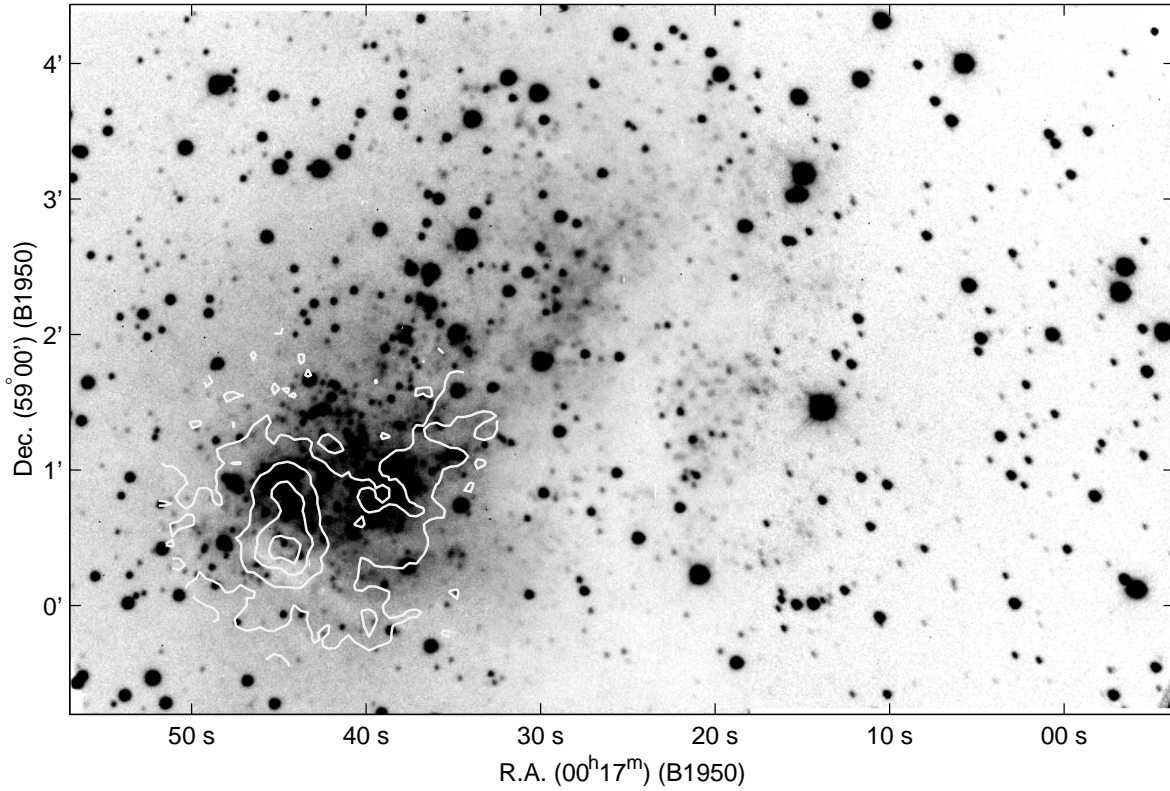


Fig. 6.— IC 10 in a B band mosaic obtained at the Lowell Observatory 72" Perkins telescope in Anderson Mesa, Arizona, with the SCUBA map overlaid. The dust continuum is strongest along an obscuration lane that corresponds to the peak of the H I map of Shostak & Skillman (1989). The void region near $00^{\text{h}}17^{\text{m}}25^{\text{s}}$, $59^{\circ}01'30''$ corresponds to hole no. 2 in the same paper, while the empty region close to $00^{\text{h}}17^{\text{m}}20^{\text{s}}$, $59^{\circ}02'30''$ is probably associated with another of the H I peaks.

850 μm and 155 μm continuum

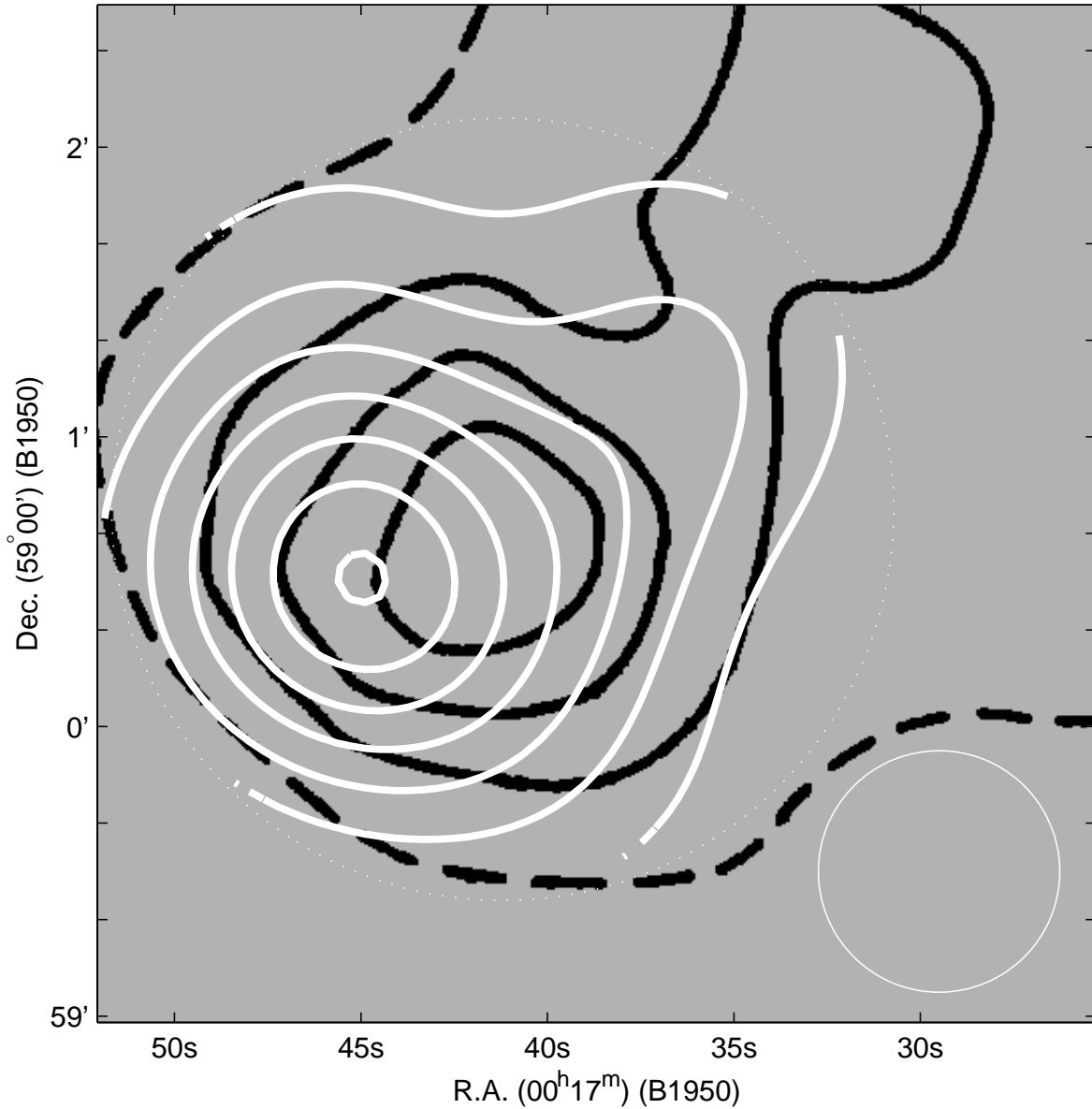


Fig. 7.— Previous KAO 155 μm observations (Thronson et al. 1990, black contours) compared with our SCUBA 850 μm map convolved to a 50'' beam size (white contours). The displacement is most likely due to pointing discrepancies with the KAO. The convolved SCUBA contour levels are 100 to 700 in steps of 100 mJy per 50'' beam. The contours in the 155 μm data are 5, 10 and 15 Jy per 50'' beam. The dotted circle shows the approximate area mapped by SCUBA, while the white thin circle in the lower right corner shows one 50'' beam.

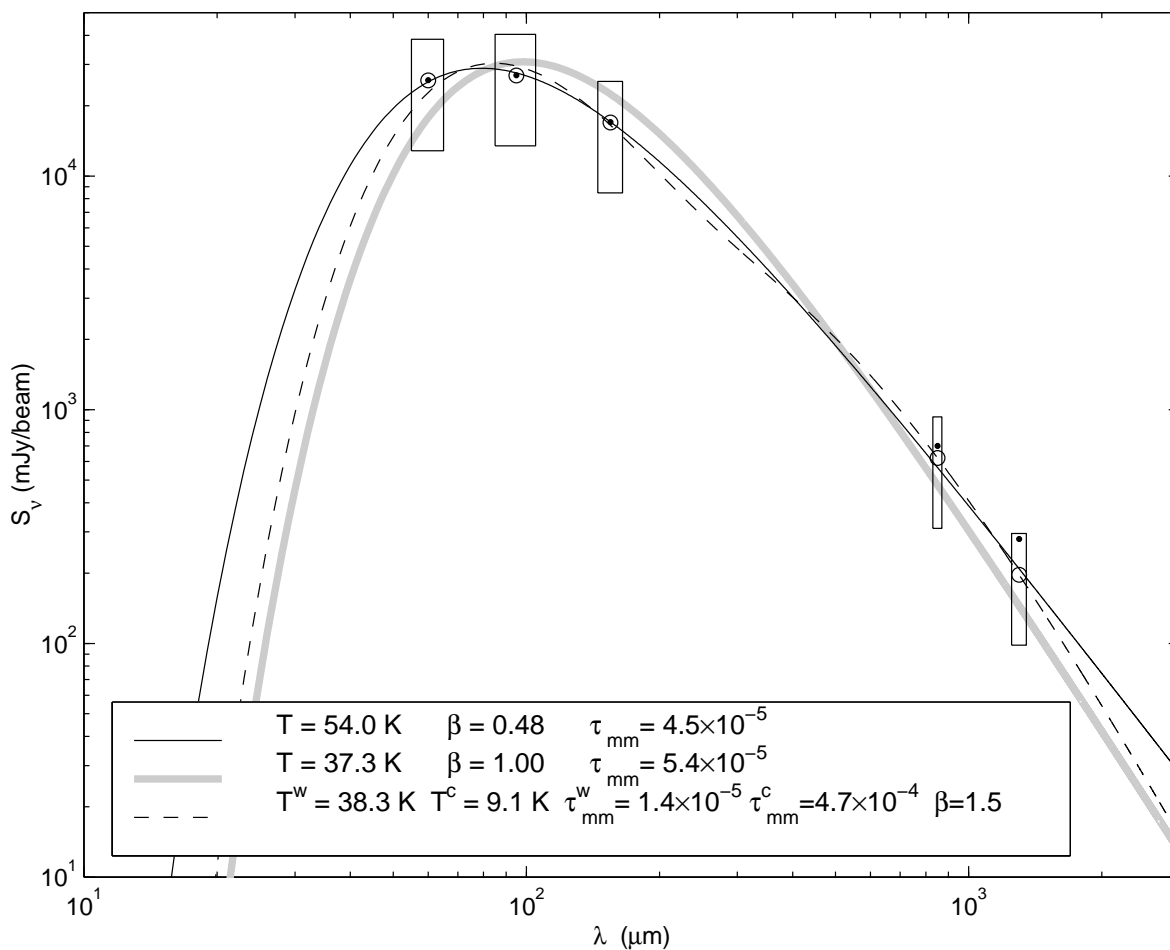


Fig. 8.— Flux density distribution of IC 10-SE in the FIR-submillimeter region, showing the fits to the 60, 95, 155, 850 and 1300 μm free-free corrected data (small circles). The original measurements are shown here by black dots. The 3σ error boxes are those in Table 4. The main graybody solution (black solid line), with emissivity exponent $\beta \sim 0.5$, is shown here together with the best $\beta = 1$ fit and the two-temperature solution for $\beta = 1.5$.

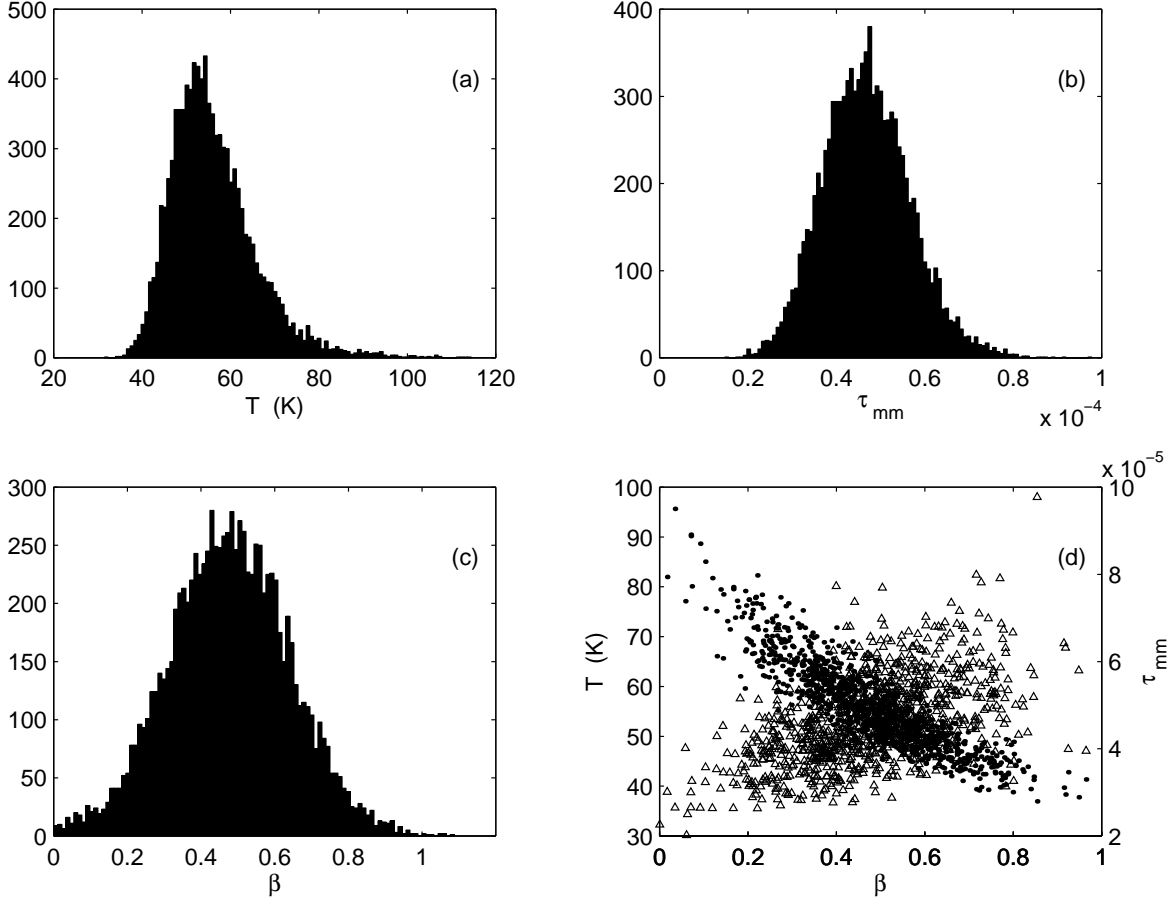


Fig. 9.— 10^4 point Monte Carlo error analysis for the graybody solution derived using the combined KAO, SCUBA and IRAM measurements described in the text. All the solutions with $\beta < 0$ (about 19%) were considered unphysical and removed from the plots and the distributions before computing the median and the error estimates. The histograms (a), (b), and (c) show the distribution of the solutions for the graybody parameters: T , τ_{mm} and β . The scatter plot (d) shows about 10% of the solutions for T (dots) and τ_{mm} (triangles) plotted against their emissivity exponent, β . Thus, high temperature and low τ_{mm} occur for low β . The mm opacity τ_{mm} is relatively insensitive to the values of the other parameters in the graybody solution.

Table 1. Measured [C I] line parameters for IC 10-SE

	R.A. (B 1950)	Dec (B 1950)	T_{mb} ^{a,b} (K)	V_{LSR} ^b (km s ⁻¹)	FWHM ^b (km s ⁻¹)	$I_{[C I]}$ ^{a,c} (K km s ⁻¹)	RMS ^d (K)	τ_{int} ^e (s)
MC 1	00 ^h 17 ^m 44 ^s .3	59°00′25″	0.41±0.06	-329.6±0.4	6.9±1.0	2.92±0.37	0.13	5400
MC 2	00 ^h 17 ^m 45 ^s .0	59°00′19″	0.35±0.06	-328.9±0.5	6.9±1.3	2.56±0.39	0.13	5400
MC 3	00 ^h 17 ^m 44 ^s .0	59°00′15″	0.21±0.06	-330.6±1.1	9.6±2.7	2.23±0.50	0.13	4500
SL 1	00 ^h 17 ^m 43 ^s .7	59°00′39″	0.37±0.75	0.19	1800
SL 2	00 ^h 17 ^m 44 ^s .0	59°00′33″	0.25±0.08	-332.1±1.3	8.3±2.5	2.19±0.63	0.13	5040
SL 3	00 ^h 17 ^m 44 ^s .8	59°00′15″	0.32±0.88	0.22	1800

^aErrors are 1σ , statistical. Systematic 3σ calibration uncertainty is estimated to be $\sim \pm 30\%$.

^bValues and errors derived from gaussian fit.

^cIntegrated over a \pm FWHM range around the V_{LSR} velocity. The CO ($J = 3 \rightarrow 2$) V_{LSR} and FWHM were used for the [C I] non-detections.

^dBaseline RMS. Computed using 3 MHz spectral resolution and scaled to T_{mb} .

^eTotal accumulated integration time including on+off positions.

Table 2. Measured ^{12}CO line parameters for IC 10-SE

	$^{12}\text{CO} (J = 3 \rightarrow 2)$						$^{12}\text{CO} (J = 1 \rightarrow 0)$	
	T_{mb} ^{a,b} (K)	V_{LSR} ^b (km s ⁻¹)	FWHM ^b (km s ⁻¹)	I_{CO} ^{a,f} (K km s ⁻¹)	$I_{[\text{C I}]} / I_{\text{CO}}$ ^{d,g}	$\frac{\Delta v_{\text{CO}}}{\Delta v_{[\text{C I}]}}$ ^e	I_{CO} ^c (K km s ⁻¹)	$I_{[\text{C I}]} / I_{\text{CO}}$ ^d
MC 1	1.66±0.02	-329.7±0.1	13.2±0.2	22.8±0.8	0.13±0.02	1.9±0.3	14.3	0.20±0.04
MC 2	1.24±0.03	-327.4±0.2	15.0±0.5	19.0±0.5	0.13±0.03	2.2±0.4	11.7	0.22±0.05
MC 3	0.77±0.03	-336.5±0.4	18.5±0.9	14.9±0.6	0.15±0.04	1.9±0.5	9.4	0.24±0.06
SL 1	0.41±0.06	-332.6±0.6	8.1±1.3	3.4±0.5	0.11±0.22	...	0.3	< 2.50±2.70
SL 2	1.33±0.05	-330.7±0.2	9.9±0.4	13.8±0.5	0.16±0.05	1.2±0.4	5.5	0.40±0.13
SL 3	0.88±0.04	-327.9±0.4	17.0±0.8	15.5±0.6	0.02±0.05	...	7.8	< 0.11±0.12

^aErrors are 1σ , statistical. Systematic 3σ calibration uncertainty is estimated to be $\sim \pm 30\%$.

^bValues and errors derived from gaussian fit.

^cOVRO integrated intensity convolved to JCMT [C I] beam size. Its systematic 3σ calibration uncertainty is estimated to be $\sim \pm 30\%$.

^dThe 1σ error in the ratio includes the 10% 1σ calibration uncertainty as well as the statistical errors.

^eRatio of linewidths computed as ratio of the corresponding FWHM.

^fIntegrated over a $\pm\text{FWHM}$ range around the V_{LSR} velocity.

^gNot corrected for beam size difference.

Table 3. Measured $^{13}\text{CO} (J = 3 \rightarrow 2)$ line parameters for IC 10-SE

	T_{mb} ^{a,b} (K)	V_{LSR} ^b (km s ⁻¹)	FWHM ^b (km s ⁻¹)	I_{CO} ^a (K km s ⁻¹)	$I_{^{12}\text{CO}} / I_{^{13}\text{CO}}$	RMS ^d (K)
MC 1	0.17±0.03	-331.7±1.0	10.7±2.4	2.0±0.4	11.4±2.3	0.06
MC 2	0.11±0.03	-331.2±1.9	15.2±4.5	1.9±0.4	10.0±2.1	0.06
MC 3	0.11±0.03	-337.0±2.7	20.6±6.5	2.5±0.6	6.0±1.5	0.07
SL 2	0.3±0.5 ^c	46 ^e	0.07

^aErrors are 1σ , statistical. Systematic 3σ calibration uncertainty is estimated to be $\sim \pm 30\%$.

^bValues and errors derived from gaussian fit.

^cIntegrated over the velocity extent of the ^{12}CO line.

^dBaseline RMS. Computed using 3 MHz spectral resolution and scaled to T_{mb} .

^eFormal errors are ${}_{-29}^{+\infty}$.

Table 4. Continuum measurements for IC 10-SE

Wavelength ^a (μm)	Flux ^{a,b} (Jy)	Telescope	Reference
60 \pm 5	25.7 \pm 12.8	IRAS HIRES ^c	This paper
95 \pm 10	27 \pm 13.5	KAO	Thronson et al. 1990
155 \pm 10	17 \pm 8.5	KAO	Thronson et al. 1990
850 \pm 30	0.70 \pm 0.35	JCMT	This paper
1300 \pm 50	0.28 \pm 0.14	IRAM	Wild 1998

^aErrors are 3σ estimates.

^bFlux measured in a $50''$ HPBW beam. Errors correspond to adopted $\pm 50\%$ 3σ calibration uncertainty.

^cFlux in a $60'' \times 50''$ HPBW beam with P.A.= 38° . HIRES resolution after 60 iterations is $56'' \times 35''$ with P.A.= 38° .

Table 5. Continuum solutions for IC 10-SE

Temperature (K)	τ_{mm}	β	$N_{\text{H}} \cdot b$ (cm^{-2})	Comments
58.6	5.2×10^{-5}	0.31	2.9×10^{22}	general graybody solution
54.5 ^{+43.6} _{-17.1}	$4.6^{+3.2}_{-2.4} \times 10^{-5}$	$0.48^{+0.46}_{-0.44}$	$2.8^{+1.9}_{-1.4} \times 10^{22}$	graybody with $S_{\nu}^{ff} = 80 \cdot \lambda_{\text{mm}}^{0.15}$ mJy removed ^a
38.3	1.4×10^{-5}	1.5	8.1×10^{21}	two components model with fixed β
9.1	4.7×10^{-4}	1.5	2.6×10^{23}	
53.2	1.2×10^{-5}	1.0	6.5×10^{21}	two components model with fixed β
20.9	1.1×10^{-4}	1.0	6.4×10^{22}	
33.2	8.5×10^{-6}	2.0	4.7×10^{21}	two components model with fixed β
6.5	1.1×10^{-3}	2.0	6.4×10^{23}	

^aErrors are 3σ estimates based on a Monte Carlo analysis. Central values are computed as the median of the Monte Carlo distribution.